The Full Diurnal Cycle of Mars Water-Ice Cloud Optical Depth in EMIRS Observations

Samuel A. Atwood[1,2,3], Michael D. Smith[2], Michael J. Wolff[4], Christopher S. Edwards[5]

[1]University of Maryland Baltimore County, Baltimore, MD, USA
[2]NASA Goddard Space Flight Center, Greenbelt, MD, USA
[3]Center for Research and Exploration in Space Science and Technology, NASA/GSFC, Greenbelt, MD, USA
[4]Space Science Institute, Boulder, CO, USA
[5]Department of Astronomy and Planetary Science, Northern Arizona University, Flagstaff, AZ, USA

Corresponding author: Sam Atwood (samuel.a.atwood@nasa.gov)

Key Points:

- Improved analysis of Mars thermal infrared spectra enabled retrieval of water ice cloud optical depth across the full diurnal cycle
- Observations showed higher water ice cloud abundance at night compared to day, with distinct peaks in early morning and evening hours
- Evening clouds were broadly distributed across low latitudes, while morning clouds were more concentrated over the Tharsis region

Abstract

Improvements to analyses of Martian thermal infrared spectra observed by the Emirates Mars Infrared Spectrometer (EMIRS) allow for retrieval of water-ice cloud optical depth, τ_{ice}, across the full diurnal cycle at Mars. Using observations spanning nearly two Martian years, we find a persistent pattern of higher nighttime cloud abundance compared to daytime values, with regular peaks in τ_{ice} occurring in both morning and evening hours. During the colder aphelion season when the low-latitude aphelion cloud belt forms, zonal mean optical depths ranged from maxima of ~0.5 during the morning peak to minima of ~0.15 near midday. Averaged across the full dataset, nighttime τ_{ice} values were approximately twice the optical depth at the midday minimum. The morning peak in cloud abundance tended to occur near a solar incidence angle of 75° across a range of latitudes and seasons. These diurnal patterns were generally consistent with modeled influences of atmospheric thermal tides on cloud formation conditions. Spatial differences in the distribution of clouds were noted across the diurnal cycle. Volcano clouds formed near midday and increased in optical depth throughout the afternoon and into the evening. At night, late evening clouds were observed more broadly across low-latitude regions, while morning clouds were more concentrated over the Tharsis region. The broad spatial and temporal coverage of these results enables new model comparisons against observations of τ_{ice} across the full diurnal cycle, and advances our understanding of water-ice cloud development and its role in the Mars climate system.

Plain Language Summary

Water-ice clouds are one of the most variable components of Mars' atmosphere. The abundance of these clouds changes across both daily and seasonal timescales, with notable variations occurring near surface features like volcanoes and large basins. Many previous observations were conducted near the middle of the day when these clouds are generally thinnest. Using new observations from the Emirates Mars Infrared Spectrometer (EMIRS) onboard the Emirates Mars Mission (EMM) spacecraft, we can now observe these clouds throughout the full Martian day and night. Looking at nearly two Martian years of observations, we found that clouds are typically thicker at night than during the day, with additional peaks in cloudiness occurring in the early morning and evening hours. Some of the thickest clouds form in a band near Mars' equator during the planet's cold season, reaching their daily maximum thickness shortly after sunrise. During this season, clouds in the late evening were found to be spread more widely across low latitudes, while early morning clouds were concentrated over a region called Tharsis. These results provide the first comprehensive observations of nighttime clouds on Mars, helping to validate atmospheric models and improve our understanding of how water moves through the Martian atmosphere.

1 Introduction

Water-ice clouds are among the most variable components of the Martian atmosphere over diurnal and spatial scales. Patterns of atmospheric temperature fluctuations driven by solar heating and thermal tides alter the environmental water saturation ratios that modulate cloud development (Zurek, 1976; Barnes et al., 2017; Clancy et al., 2017). This results in a noted coupling between the temperature profile and radiatively active water-ice clouds that vary throughout the full diurnal cycle of a Martian solar day (sol) (Madeleine et al., 2012b; Kleinböhl et al., 2013; Wilson & Guzewich, 2014; Szantai et al., 2021). At synoptic scales, variability in

cloud abundance has been linked with global circulation patterns that are affected by both dynamical processes and large-scale topography, in addition to the behaviors driven by diurnal and semi-diurnal thermal tides. At smaller scales, local topographic effects and small-scale circulations, such as those over volcanoes, can yield large spatial gradients in cloud abundance (Michaels et al., 2006; Wilson et al., 2007). In addition to these drivers of variability, water-ice clouds are themselves important factors controlling global circulation, radiative transfer, and the hydrologic cycle on Mars (Clancy et al., 2017; Montmessin et al., 2017; Määttänen & Montmessin, 2021). However, uncertainty remains over the temporal and spatial scales across which these clouds vary—particularly at night—leading to challenges in adequately modeling water-ice cloud and its effects in global circulation models (Määttänen & Montmessin, 2021), and in understanding the full role they play in the Mars planetary system.

Observations of variability in water-ice clouds began with terrestrial instruments and early spacecraft imagers and spectrometers on the Mariner and Viking missions, which provided the first indications of complexity across both spatial and temporal scales (e.g., Curran et al., 1973; French et al., 1981; Kahn, 1984). Quantification of water-ice cloud abundance across seasonal, inter-annual, and spatial dimensions was obtained from the Thermal Emission Spectrometer (TES) onboard the Mars Global Surveyor (MGS) orbiter, which produced the first detailed cloud climatologies as retrieved water-ice optical depth (τ_{ice}) (Smith, 2004). Numerous additional observational datasets have followed that expanded upon these results using instruments that observe across ultraviolet, optical, and infrared wavelengths (reviewed by Clancy et al., 2017 and Määttänen & Montmessin, 2021)—yielding additional resolution and coverage, along with identification of new cloud morphologies, behaviors, and interactions. Among the findings of these results has been the identification of a seasonal water-ice cloud cycle that includes increases in cloud abundance during the colder aphelion season and decreases during the warmer and dustier perihelion season. Several cloud types have also been identified, with the most prevalent being those associated with the low-latitude aphelion cloud belt (ACB) and polar cap clouds that occur during the winter season in each hemisphere. However, many of these results were obtained from sun-synchronous instruments that observe at or near the same local true solar time (LTST) for all data points, leading to climatologies that are biased towards classification of afternoon behavior.

Information on the diurnal variability in water-ice clouds was generally more limited in early observational datasets, with some information on daytime variability produced from the Viking IRTM (Tamppari et al., 2003), and MGS Mars Orbiter Camera (Benson et al., 2003) instruments. More recent missions have begun to provide additional observations of daytime diurnal variability. Slowly migrating diurnal coverage from spacecraft such as Mars Express and Mars Odyssey have provided some information on daytime diurnal variability (e.g., Madeleine et al., 2012a; Smith, 2019)—though the slow orbital migration has led to the seasonal water-ice cloud signal being convolved with the diurnal signal. Additional diurnal observations have been provided at locations from surface missions (e.g., Kloos et al., 2018; Hayes et al., 2024; Smith et al., 2025). From these, a general conceptual picture of water-ice cloud daytime diurnal variability has emerged. In the case of clouds not associated with the seasonal polar cap clouds—between roughly 60 S and 60 N latitude, and occurring throughout the year but at greater magnitudes during aphelion season when they are associated with the ACB—water-ice clouds abundance generally reaches a minimum just after midday, with higher τ_{ice} often observed in the mornings and afternoons (e.g., Smith, 2009, 2019; Pankine et al., 2013; Wolff et al., 2019, 2022; Giuranna et al., 2021; Szantai et al., 2021; Atwood et al., 2022, 2024). However, systematic diurnal

coverage necessary to validate and quantify this behavior has not been available until the Emirates Mars Mission (EMM)—which features observations from a spacecraft placed into a higher orbit suitable for systematic diurnal observations on sub-seasonal timescales.

Information about nighttime cloud abundance has been considerably more limited in most observational datasets, but has generally indicated higher water-ice optical depths during the night as compared to the day. Among the first indirect observational evidence for this behavior was data from studies that examined surface and atmospheric temperature anomalies at night. Wilson et al., (2007) used an atmospheric model with radiatively active water-ice clouds to attribute anomalously warm nighttime surface temperatures retrieved from some TES nighttime observations (~02:00 LTST) to increased downward infrared radiation from more abundant nighttime clouds. Similar indirect studies of coupling between atmospheric temperature profiles and water-ice cloud suggested higher nighttime cloud abundance would be expected given observed temperatures (Hinson & Wilson, 2004; Kleinböhl et al., 2013; Wilson & Guzewich, 2014). Direct observations of τ_{ice} at night have been obtained predominately from thermal infrared spectrometers, though such observations are less sensitive at night and subject to higher uncertainties (Pearl et al., 2001). Efforts to retrieve atmospheric opacities from TES nighttime observations have previously suggested higher τ_{ice} at night as compared to the day (Pankine et al., 2013). Similar observations from the Planetary Fourier Spectrometer (PFS) onboard the Mars Express orbiter averaged into general "daytime" and "nighttime" bins showed similarly higher observed τ_{ice} at night, along with some evidence for morning and afternoon peaks in abundance in ACB clouds, though with considerable variability still noted (Giuranna et al., 2021). Results from both TES and PFS showed differences in the spatial patterns of variability between day and night, but had insufficient diurnal and spatial coverage to capture the full behavior of nighttime clouds. Most recently, observations across the full diurnal cycle from the Thermal InfraRed Sensor (TIRS) on the Perseverance rover have found higher nighttime water-ice optical depths and a regular diurnal cycle to cloud behavior at Jezero crater through nearly two Mars Years of surface based measurements (Smith et al., 2025).

Modeling efforts have highlighted the importance of thermal tides in driving large-scale development of water-ice clouds, particularly at night, as well as the influence of radiatively active water-ice clouds on diurnal variability in the Mars surface-atmosphere system (e.g., Hinson & Wilson, 2004; Madeleine et al., 2012b; Kleinböhl et al., 2013; Navarro et al., 2014; Pottier et al., 2017). Szantai et al., (2021) used the Mars Planetary Climate Model (PCM) to demonstrate diurnal patterns in water ice cloud abundance, correlating them with water ice cloud proxy measures from OMEGA spectra images. These models not only corroborated observed daytime variability but also predicted early morning peaks in water ice cloud abundance—attributing them to the influence of thermal tides—and the potential for greater cloud abundance at night. Despite these advancements, a comprehensive observational dataset spanning the full diurnal cycle of water-ice cloud necessary to validate many of these findings has been lacking (Määttänen & Montmessin, 2021).

In this study we focus on extending the observational record of variability in Mars water-ice cloud optical depth to include the first detailed coverage of the full diurnal cycle for low- and mid-latitude regions using thermal infrared observations from the Emirates Mars Infrared Spectrometer (EMIRS) onboard the Emirates Mars Mission (EMM) spacecraft. We first discuss the details of EMM observational coverage and the EMIRS dataset in section 2. This is followed by a discussion of the updated EMIRS retrieval algorithm and uncertainties in section 3,

including the implications and challenges associated with nighttime retrievals. Results are then presented in section 4 with a focus on the full diurnal cycle of τ_{ice} shown across both spatial and seasonal scales for observations that span nearly two Martian years. In section 5 we compare the EMIRS results against other diurnal observations of water-ice cloud from the EXI imager that is also on-board EMM, and the TIRS instrument on the Perseverance rover. Finally, in section 6 we include a brief conclusion with a summary of the results and discussion of their potential use for future model comparisons. Data archive files that accompany this study include gridded products intended to better facilitate such comparisons.

2 EMIRS dataset

EMIRS is a thermal infrared spectrometer onboard the Emirates Mars Mission (EMM) spacecraft (Almatroushi et al., 2021; Amiri et al., 2022). Observations produce spectra that include wavenumbers between approximately 100 and 1600 cm^{-1} (wavelengths between 100 and 6 μm) with a selectable spectral resolution of either 5 or 10 cm^{-1} (Edwards et al., 2021). The instrument's projected observation footprint is elliptical, with the size of its major axis varying from approximately 100 to 300 km due to changes in spacecraft height and observation angle. The EMM spacecraft occupies a unique high-altitude, low-inclination elliptical orbit that varies between approximately 20,000 and 43,000 km. This orbital configuration allows for observations across all local times and nearly all latitudes and longitudes. EMIRS conducts raster scans of the Martian disk at various points in the 55-hour orbital period, typically achieving coverage across all local times and longitudes in roughly four orbits, or approximately 5° of solar longitude (L_s) on average. The result is a synoptic view of Mars with broad spatial and temporal coverage, and a resolution that allows for global and regional scale changes to be observed over periods of about two weeks. This allows for investigation of key aspects of diurnal variability in the Martian atmosphere, though shorter-timescale phenomena such as planetary waves may introduce variability that is not fully resolved in EMIRS observations. Standard retrieved properties include temperatures at the surface and for the atmospheric profile, optical depths for atmospheric dust and water-ice aerosol, and the column abundance of water vapor (Smith et al., 2022).

The dataset used in this study spans from the beginning of the EMM science phase at $L_s \approx 49°$ in Mars Year (MY) 36 through $L_s \approx 347°$ in MY 37 (approximately May 2021–October 2024). This period encompasses two aphelion seasons, allowing for inter-annual comparison of this climatologically significant period. Short gaps in the dataset exist due to spacecraft safe modes and a solar conjunction, during which no observations were made. Data from all local times were included in these analyses. All observations that passed initial quality control checks and had emission angles less than 70° were processed through the updated retrieval algorithm described further in the next section. Of these, approximately 2,040,000 retrievals yielded valid τ_{ice} values and were included in subsequent analyses.

3 EMIRS retrieval algorithm

The retrieval algorithm is based on the constrained linear inversion approach originally developed for TES (Conrath et al., 2000; Smith, 2004; Smith et al., 2006), which retrieves atmospheric state parameters that best match each observed spectrum. Subsequent refinements were made to take advantage of the extended spectral range available in EMIRS observations and to improve treatment of surface thermophysical effects (Smith et al., 2022; Atwood et al.,

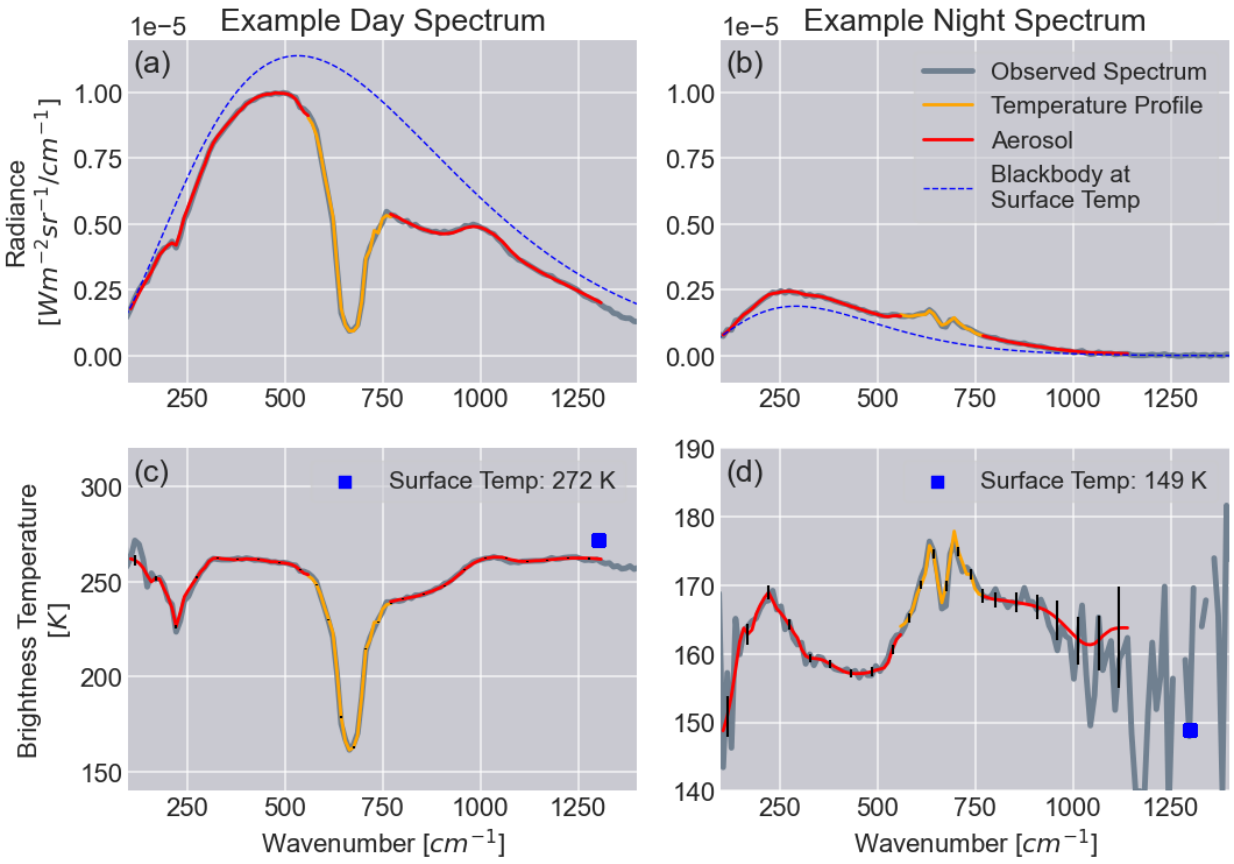

Figure 1 Example EMIRS spectra for typical day (a,c) and night (b,d) observations with the presence of water-ice clouds. Observed spectra (grey lines) are shown as radiance (a,b) and equivalent brightness temperature (c,d). Orange and red lines show the forward model best-fit spectra for the regions of the spectrum used for the temperature profile and aerosol retrieval steps, respectively. The nominal surface temperature, retrieved at 1300 cm^{-1}, is indicated with a blue box. A reference blackbody at this temperature is shown as the dashed blue line in the radiance plots. Black error bars in c&d show the wavenumber dependence of observation uncertainty as noise equivalent spectra radiance (NESR) converted to brightness temperature.

2024). The algorithm utilizes a forward radiative transfer model that includes multiple scattering by aerosol particles to generate a spectrum that is then compared against observed EMIRS level 2 calibrated radiance spectra. Figure 1 illustrates example EMIRS spectra and associated best-fit forward model results for both day and night observations as both radiance and equivalent brightness temperature spectra. State parameters in the forward model are adjusted to achieve a best fit to the observations (grey lines) via a two-step procedure. First, the atmospheric temperature profile is retrieved from the CO_2 band centered at 667 cm^{-1} (orange lines). Subsequently, dust and water-ice optical depths are retrieved using portions of the spectrum between 100 and 1315 cm^{-1}, excluding the CO_2 band (red lines). Surface temperature is also retrieved near 1300 cm^{-1} during the second step (blue squares). For reference, radiance from a blackbody at the retrieved surface temperature is shown in the radiance plots as a dashed blue line.

Water-ice optical depth is retrieved as normal-incidence column-integrated full extinction values referenced to 825 cm^{-1}. In the forward model, water-ice is distributed around an estimated condensation layer (Smith, 2004; Atwood et al., 2022; Smith et al., 2022). However, given the column integrated nature of the optical depth retrieval and large observation footprint relative to typical cloud scales (e.g., Olsen et al., 2021; Patel et al., 2023), individual τ_{ice} data points may still include clouds at multiple layers or water-ice associated with more diffuse hazes distributed across wider vertical regions. Previous work with this retrieval has indicated that uncertainty in τ_{ice} associated with uncertainties in the vertical distribution of water-ice was generally less than 0.03 across seasonal average values (Atwood et al., 2022). For the results presented here, we focus on retrieved τ_{ice} and τ_{ice} uncertainty, along with validation using additional parameters as discussed below.

3.1 Surface thermophysical parameters

Surface thermophysical effects are incorporated into the forward model as spectrally dependent emissivity properties drawn from lookup tables originally developed for TES (Bandfield, 2002). Several additional empirical correction parameters are used in the forward model to correct for expected deviations from these values. Surface anisothermality across the relatively large

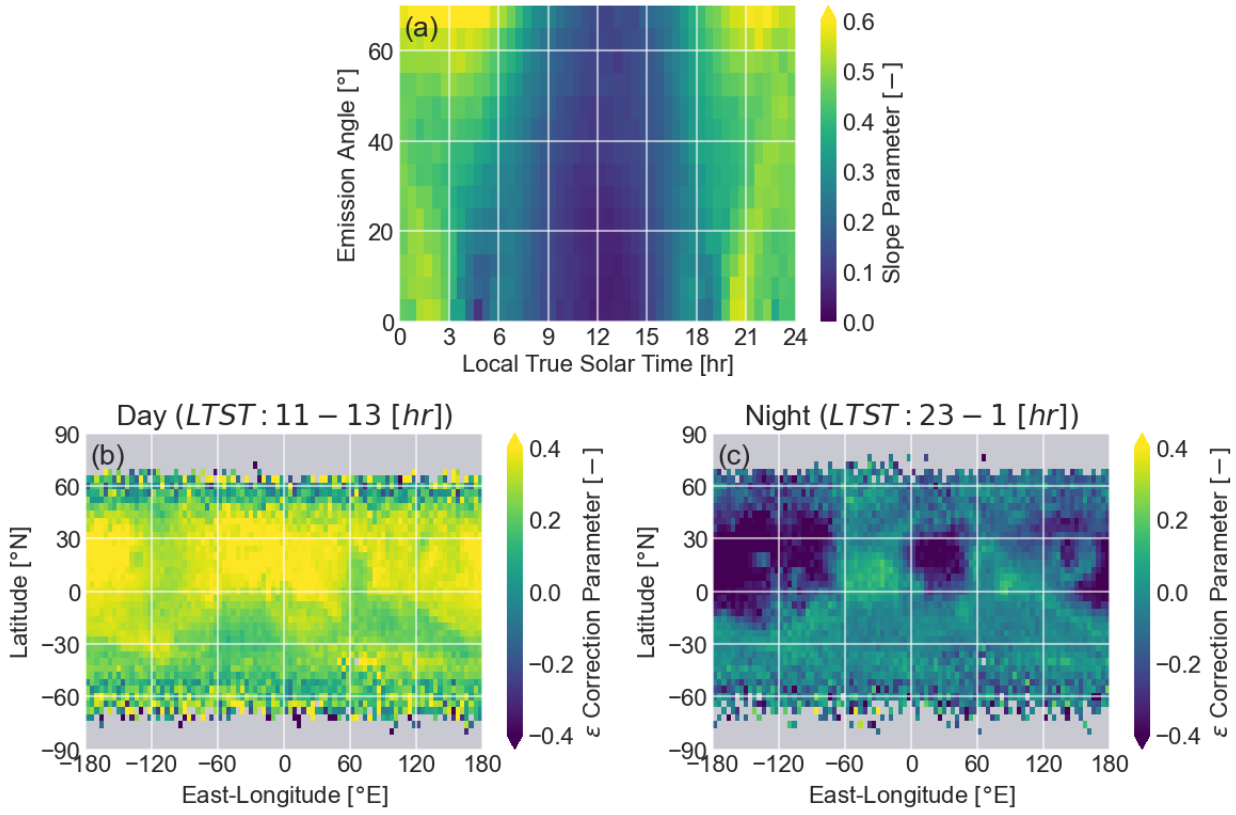

Figure 2 Mean values for surface thermophysical parameters used in the retrieval to correct for variability in observed spectra not directly accounted for in the forward model. (a) The linear slope parameter associated with variable surface temperature within an observation footprint. (b & c) The emissivity correction parameter during the day and night, respectively, showing similar patterns with known surface albedo and thermal inertia properties.

EMIRS observation footprint leads to slopes in the observed brightness temperature spectra (Bandfield & Edwards, 2008; Bandfield, 2009), which were parameterized via a linear slope parameter. An additional emissivity correction parameter was developed that applies to low wavenumbers where TES spectral data was limited and more uncertain due to a narrower spectral range and increased uncertainties below roughly 250 cm^{-1} as compared to EMIRS (Atwood et al., 2024). The resulting forward model radiance equation is discussed further in Smith (2004) and Smith et al. (2022), with updates that include details on the slope and emissivity parameters described in Atwood et al. (2024). Figure 2 illustrates the variability in these surface thermophysical parameters in retrievals for the EMIRS dataset.

Mean values for the slope parameter are shown as a function of LTST and emission angle in Figure 2(a). During midday, the diurnal cycle of surface heating from solar insolation led to more stable and homogeneous surface temperatures, resulting in lower values for this parameter (minimal spectral slope effect). At other local times, features within the observation footprint with different thermal inertias, albedos, or other properties exacerbated thermal inhomogeneities, resulting in larger values for the slope parameter. Higher emission angles, which yield both larger observation footprints and therefore potentially more regions with different temperatures, as well as increased spectral slopes when surface roughness or rock abundance are high (Nowicki & Christensen, 2007; Bandfield & Edwards, 2008; Bandfield, 2009), were also associated with larger slope parameter values.

The emissivity correction parameter is shown for midday (LTST 11:00–13:00) and midnight (LTST 23:00–01:00) mean values in Figures 2(b) and 2(c), respectively. During the day the pattern of variability showed similar characteristics to surface albedo, while during the night it more closely resembled that of thermal inertia (e.g., Jakosky et al., 2000; Nowicki & Christensen, 2007; Putzig & Mellon, 2007). While further investigation of the relationship of these empirical parameters to surface properties is beyond the scope of this work, we note that the results support classification of this variability as driven by thermophysical properties of the surface rather than unaccounted for atmospheric effects. Additional discussion and information about both of these parameters can be found in Atwood et al. (2024).

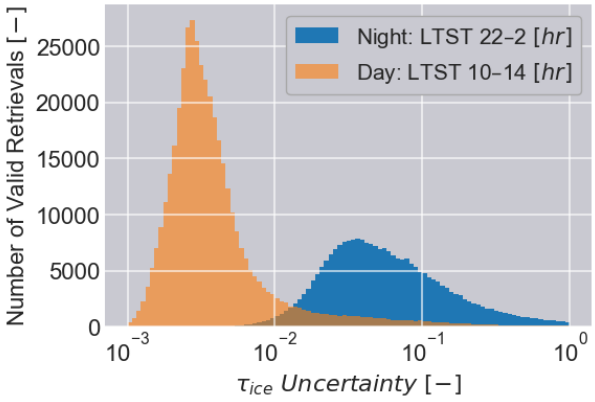

Figure 3 Histogram of water-ice optical depth uncertainty for all valid retrievals during daytime (LTST = 10:00 – 14:00 [hr]) and nighttime (LTST = 22:00 – 2:00 [hr]) observations.

3.2 Nighttime retrievals

Nighttime retrievals of thermal infrared spectra present unique challenges due to lower observed radiance and reduced thermal contrast between the surface and atmosphere (illustrated in Figures 1b&d, respectively). These factors result in decreased sensitivity to water-ice cloud properties and increased uncertainty in the τ_{ice} values. Primary sources of uncertainty are related to the observation signal-to-noise ratio and thermal contrast, with additional important factors related to surface thermophysical effects (e.g. thermal inertia and albedo, among others), errors in cloud vertical distributions, and variability in water ice particle size distributions (discussed further in Edwards et al., 2021; Smith et al., 2022; Atwood et al., 2024). As part of the retrieval algorithm, uncertainty in retrieved τ_{ice} is estimated using numerical sensitivity tests following the method outlined in Smith et al. (2022). This produced an estimate that accounts for both signal-to-noise ratios that vary greatly between day and night observations, and changes to thermal contrast that affect the ability of thermal infrared observations to differentiate between components of the surface and atmosphere. In daytime observations, τ_{ice} uncertainties were typically below 0.05, and often below 0.01 for observations outside of polar cap regions. Within these results, τ_{ice} values for individual spectra ranged from below 0.05, indicating minimal water-ice cloud, to values above 1 for the largest observed abundances.

The inclusion of the updated surface thermophysical parameters and the 45-μm water-ice cloud band into the EMIRS retrieval considerably improved the performance of the τ_{ice} retrievals at night. Nevertheless, τ_{ice} uncertainties ranged from less 0.001 to greater than 1 in these results (Figure 3). To accommodate the increased uncertainty while maintaining a comprehensive dataset, quality control criteria within the algorithm have been adjusted and analyses have been updated to better account for this range of τ_{ice} uncertainty values. Previous analyses focused on daytime observations using this retrieval algorithm have limited results to spectra with τ_{ice} uncertainties below 0.05 (e.g., Smith, 2004; Smith et al., 2022; Atwood et al., 2022). In this study, we utilized a τ_{ice} uncertainty threshold of 1.0, considering all retrievals below this value valid if they passed other quality control checks. This threshold value was selected to ensure inclusion of typical nighttime data (Figure 3), while still removing data points with very high uncertainties that may represent invalid data points or failures of the retrieval algorithm.

Additionally, as optical depths less than zero are not possible in the retrieval algorithm, when uncertainties are of the same scale as the optical depth values (which is particularly common at night) a potential bias in mean optical depth estimates can be introduced. To account for this in our analyses we employed an updated uncertainty-weighted averaging method that de-weights retrieved values with higher τ_{ice} uncertainty when averaging across various temporal and spatial dimensions. As the range of τ_{ice} values within each averaging grid box would be expected to be a function of both natural variability between observations and uncertainty in the observation itself, the weights applied to each retrieved spectrum are estimated as a function of both metrics.

The natural variance of τ_{ice} within a grid box, j, was estimated as the mean squared error,

$$v_{nat,j} = \frac{1}{N}\sum_{i}^{N}\left(\tau_{ice,i} - \overline{\tau_{ice}}\right)^2 \quad (1)$$

for each retrieval, i, of N total retrievals with a mean value, $\overline{\tau_{ice}}$. The expected total variance was then calculated by sums of variance for both natural variability and uncertainty, σ_i, to produce a weight for each spectrum as,

$$w_i = \frac{1}{v_{nat,j} + \sigma_i^2} \quad (2)$$

This estimate relies on the assumption that natural variability and uncertainty are uncorrelated, and that variability due to uncertainty therefore does not bias the $v_{nat,j}$ estimate within the grid box. A simple investigation of this assumption was conducted through calculation of the Pearson correlation coefficient between the τ_{ice} anomaly (i.e., $\tau_{ice,i} - \overline{\tau_{ice}}$) and the uncertainty for each datapoint. This coefficient was calculated for each of the various averaging dimensions shown below in the results sections. The correlation coefficients ranged between 0.24 and 0.32, indicating a small positive correlation between the two. However, the associated coefficients of determination (R^2) were less than 0.1—indicating that for a simple linear correlation model, no more than ~10% of the variability in $v_{nat,j}$ could be explained by σ_i^2, or vice versa. For the purposes of this weighted averaging, this was considered sufficiently independent to apply the simple sums of variance method to estimate a weighting factor. Finally, the weighted mean of τ_{ice} for each grid box was estimated as,

$$\tau_{ice,j} = \frac{\sum_i^N w_i * \tau_{ice,i}}{\sum_i^N w_i} \quad (3)$$

Two alternative averaging methods using an un-weighted mean and a weighted mean dependent only on the uncertainty (i.e., $w_i = 1/\sigma_i^2$) were also calculated for reference. During low-uncertainty periods during the day the differences between averaging methods were minimal, while differences increased at night and when uncertainties were high. Across all valid grid boxes with more than 10 data points used in the subsequent sections, and in comparison to the updated (uncertainty and natural variability weighted) method, the un-weighted mean was approximately 13% higher on average (standard deviation of the grid box percentage differences: 29%) while the uncertainty-only weighted mean was approximately 17% lower (standard deviation: 28%). Results in the following sections utilize this updated weighted-mean methodology using equations 1–3 for all τ_{ice} analyses. In addition, mean τ_{ice} uncertainty is shown

for each figure to illustrate changes in water-ice sensitivity across various dimensions and place typical uncertainty values in context.

4 Results and discussion

Results were first categorized into three seasonal periods of interest (referred to here as POI) based on typical water-ice cloud and dust conditions. The first of these was classified as a simple aphelion season average (POI 1), considered here as L_s=40°–150° in MY 36 & 37, during which the ACB was apparent and low-latitude water-ice clouds were abundant. For observations outside this L_s range, two additional categories of spectra were classified based on the amount of dust in the atmosphere (see Smith et al., 2025a, for additional discussion of τ_{dust} in these results). For periods during and just after regional dust storms, the elevated concentration of atmospheric dust warms the atmosphere and suppresses water-ice cloud formation. These periods of higher dust concentrations (POI 3) were classified as: MY 36 L_s=220°–270°, MY 36 L_s=312°–340°, MY 37 L_s=210°–270°, and MY 37 L_s=310°–325°. The final category (POI 2) included all remaining periods, and was generally classified as having lower water-ice concentrations as compared to POI 1 and lower dust concentrations as compared to POI 3.

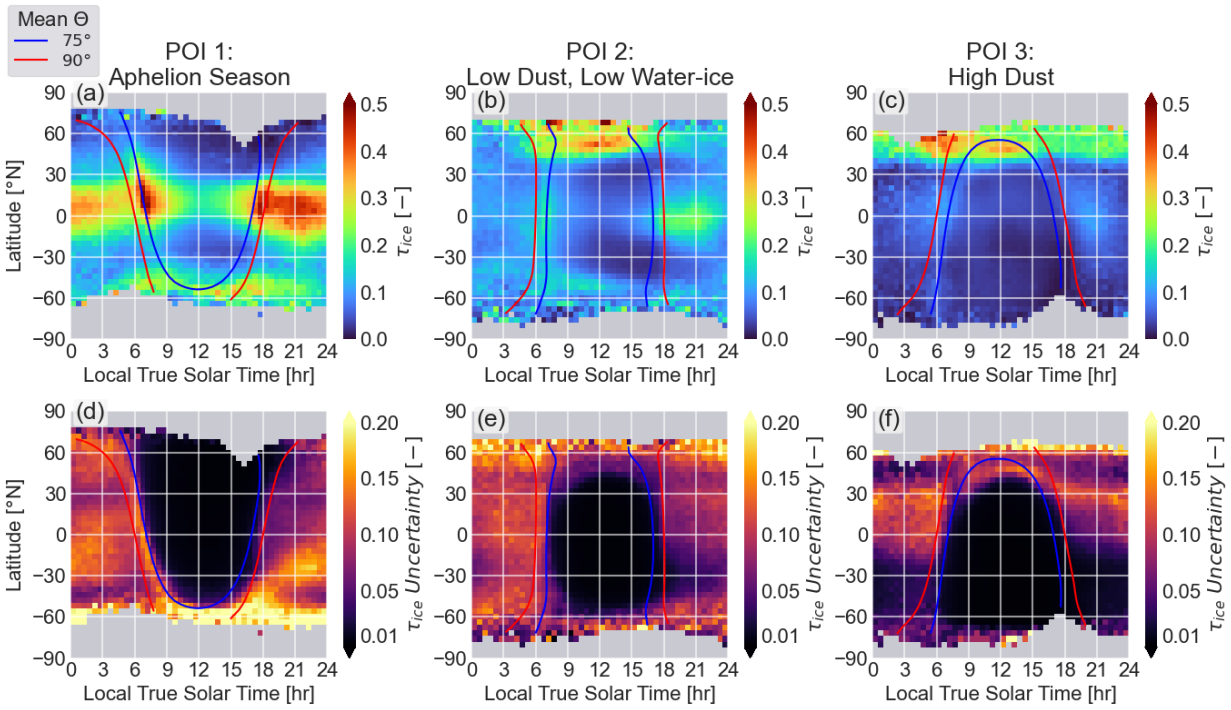

Figure 4 (a–c) EMIRS zonal mean water-ice optical depth across the full diurnal cycle for observations during (left column) POI 1: aphelion season (L_s=40°–150°), (middle column) POI 2: periods between regional dust storms, and (right column) POI 3: dusty periods during and after regional dust storms, with (d–f) associated mean uncertainties. Contour lines are shown for the mean solar incidence angle (θ) at 90° (red; the terminator between day and night) and 75° (blue).

4.1 Zonally averaged diurnal cycle

The full diurnal cycle of retrieved water-ice optical depth is shown as zonally averaged τ_{ice} values for the three periods of interest in Figure 4. During the aphelion season average (Figure 4a), a strong diurnal cycle was evident in the low-latitude ACB. The midday minimum in τ_{ice} noted in previous datasets was similarly apparent in these results. Cloud abundance began to increase from this midday minimum, including a rapid increase and small peak near the evening terminator, followed by a decreasing trend throughout the night. However, as will be discussed further below, longitudinal differences indicated the timing of this nighttime maximum in τ_{ice} varied by region. Shortly after dawn τ_{ice} again increased to the largest zonal-mean values in the diurnal cycle. Nighttime clouds were similarly highest in the low-latitudes of the ACB, but were observed with wider latitudinal extents than the daytime ACB. The daytime ACB has often been associated with clouds between roughly 10°S and 30°N latitude (e.g., Clancy et al., 2017). The nighttime ACB was somewhat wider, with equivalent τ_{ice} threshold values expanding the ACB to regions between roughly 25°S and 35°N at its maximum extent around 22:00.

The average solar incidence angle is shown in these plots for 90° (red contour line) indicating the terminator at dawn and dusk, and at 75° (blue contour line), which indicates times shortly after dawn and before dusk (15° is one Martian hour at the equator on the equinox). Interestingly, the

ACB morning τ_{ice} peak closely followed the 75° solar-incidence angle contour across a range of latitudes (Figure 4a). Zonal average τ_{ice} for 20° latitude bins are shown in Figure 5 as a function of LTST (top row), and solar incidence angle for the dawn and dusk segments (middle and bottom row, respectively). During aphelion season the local time of this early morning peak ranged by latitude from roughly 06:00 to 08:00 (Figure 5a) but was consistently near 75° solar-incidence angle (except for polar cap clouds at higher southern latitudes), indicating that the peak may be related to time since sunrise. While there was a peak in τ_{ice} during the evening for low- to mid-latitude clouds in these results, there was no evidence for a consistent relationship in the timing of that peak to either local time or solar incidence angle. Rather, the late τ_{ice} peak tended to occur between roughly sunset and midnight. Similar diurnal patterns tended to occur in POI 2 during periods between dust storms throughout the rest of the year, though at lower magnitudes. During dust storms water-ice cloud abundance was generally quite low, though a similar pattern of relative peaks in the morning and evening were present. Across the full dataset, zonal-mean

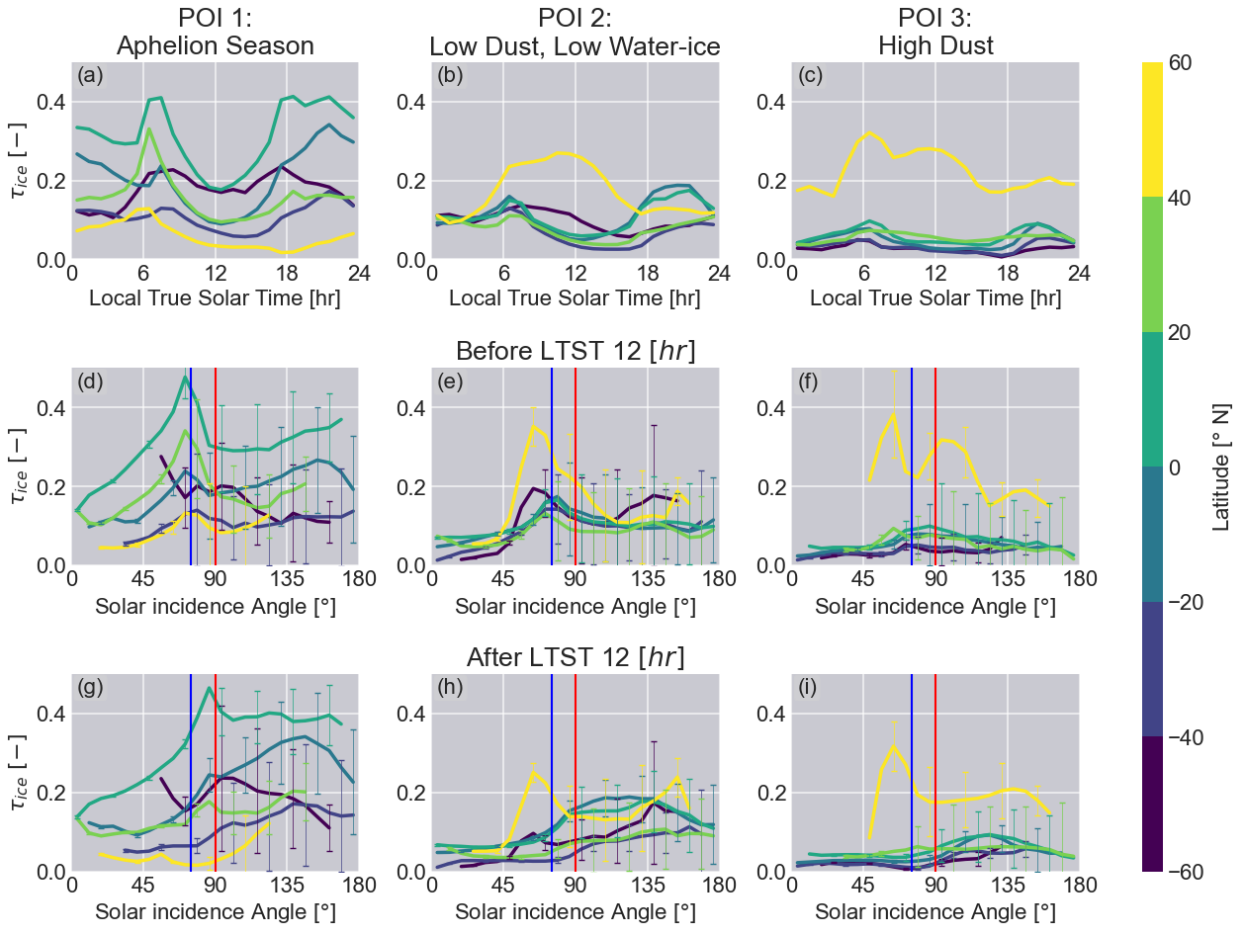

Figure 5 (a–c) EMIRS zonal mean water-ice optical depths across the full diurnal cycle for similar observation periods to Fig 3. Results are further segmented by solar incidence angle for observations before (d–f) and after (g–i) local noon. Uncertainties are shown as error bars at +/- mean uncertainty (included only on d–i to improve figure legibility) and show the generally higher uncertainties typical of nighttime (solar incidence angles > 90) observations. Vertical lines show equivalent solar incidence angles to Fig 3 at 75° and 90°.

τ_{ice} values observed at night were approximately twice their midday minimum values. This nighttime enhancement was most pronounced in the ACB where midday values of ~0.15 were contrasted with nighttime values that often exceeded 0.3.

Mean τ_{ice} uncertainty patterns shown in Figure 4 tended to follow the diurnal cycle, with generally higher uncertainties during nighttime hours. As uncertainty is primarily driven by total radiance and thermal contrast between the atmosphere and surface, some additional complexity was apparent in the patterns. A peak in uncertainty occurred just after dawn (red contour lines) during aphelion season as solar heating began warming the surface. During these times, surface temperatures tended to transition from below atmospheric temperatures to above them, resulting in reduced thermal contrast and decreased sensitivity to water-ice spectral features. Notably, the observed morning peak in τ_{ice} occurred after this uncertainty maximum, suggesting it represents a real feature rather than an artifact of retrieval uncertainty. The error bars in Figure 5, which show mean uncertainty around the zonal mean optical depth, provide additional context for comparing uncertainty magnitudes to diurnal τ_{ice} variations. For low-latitude ACB clouds in particular, while nighttime uncertainties were higher than during the day, the magnitude of the τ_{ice} variability was greater than nighttime uncertainties, supporting a robust finding of higher mean water-ice cloud abundance at night compared to day during aphelion season.

Finally, we also note that some degree of correlation between τ_{ice} and τ_{ice} uncertainty was apparent in these results, particularly at night. As noted in section 3.2, uncertainties of the same scale as optical depth (combined with a non-negative constraint on optical depth) would be expected to bias mean τ_{ice} values high. While some of this effect was removed by the updated uncertainty weighted mean method, we note that a "background" component of the nighttime optical depth signal related to increased uncertainties may still exist in these results. Nevertheless, the noted independence of major optical depth features from uncertainty features in figure 4 supports the general conclusions of these results.

4.2 Seasonal trends in the diurnal cycle

The seasonal progression of water-ice cloud optical depth is shown in Figure 6 for observations spanning from $L_s \approx 49°$ in MY 36 through $L_s \approx 347°$ in MY 37. Zonal mean τ_{ice} averaged across all local times (Figure 6a) showed patterns consistent with previous observations of the seasonal water-ice cloud cycle (e.g. Smith, 2004). Polar cap clouds were apparent in winter hemispheres, while a seasonal cycle in low- and mid-latitude clouds reached a peak during aphelion seasons ($L_s \approx 40°$-$150°$) associated with ACB clouds. However, mean τ_{ice} values in EMIRS results were higher than those reported from TES observations—which were obtained at approximately 14:00 LTST near when water-ice clouds typically reach their daily minimum. While TES maximum values for ACB clouds were around 0.15, the inclusion of all local times in these averages yielded EMIRS mean τ_{ice} values between 0.4 and 0.5 during peak ACB periods—reflecting the substantial diurnal variability and increased nighttime abundance of water-ice clouds. Additionally, EMIRS observations revealed increased cloud abundance during less dusty periods outside of aphelion season. These clouds, which formed primarily at night and were often associated with distinct evening and morning peaks, were not readily apparent in the midday TES observations.

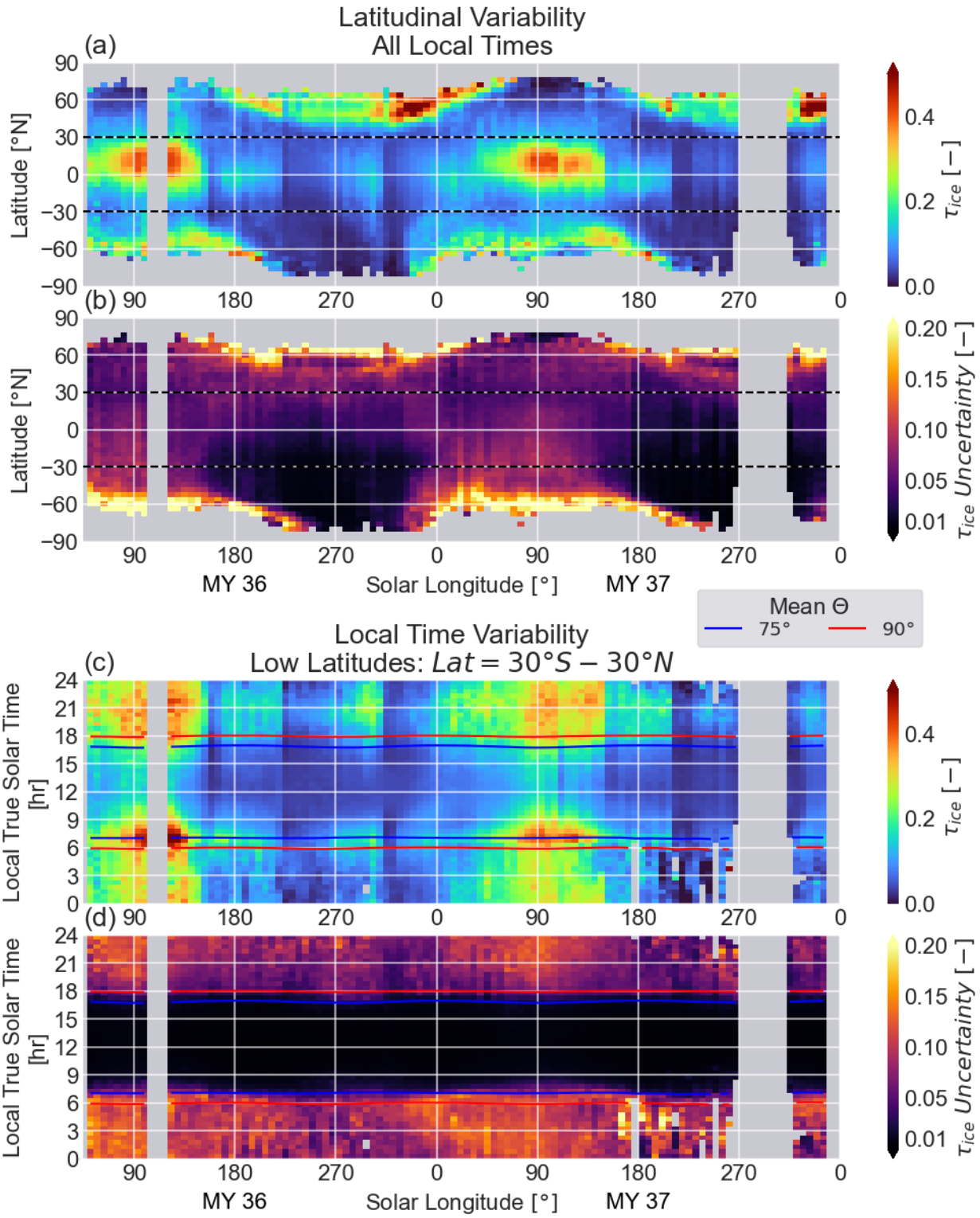

Figure 6 The seasonal progression of EMIRS water-ice optical depth and associated uncertainty, between roughly L_s=40 in MY 36 to L_s=347 in MY 37. (a,b) Zonal mean optical depth by latitude averaged across all local times. (c,d) The diurnal cycle averaged across low latitudes (30 °S – 30 °N) and all longitudes. Contour lines shown similar to Figure 3.

The diurnal cycle of τ_{ice} averaged across low latitudes (30°S – 30°N) is shown in Figure 6c. The fundamental pattern noted in the previous section—characterized by morning and evening peaks separated by a midday minimum and often higher opacities at night—persisted throughout much of the Martian year, though with considerable variation in magnitude. During aphelion seasons, low-latitude ACB clouds reached zonal mean τ_{ice} values as high as 0.5 in the early morning while dropping to ~0.15 near midday. This diurnal pattern remained detectable, but with reduced amplitude and some changes in the relative amplitudes of the morning and evening peaks, throughout much of the rest of the year. Non-aphelion season low dust periods included τ_{ice} values that exceeded 0.2, as well as some periods in which the diurnal maximum in τ_{ice} occurred during the evening peak. During regional dust storms, increased atmospheric dust loading and the associated atmospheric warming tended to suppress water-ice cloud formation at night and limit the morning and evening peaks in water-ice optical depth.

Mean uncertainties associated with these retrievals showed expected patterns of higher values during nighttime hours (Figures 6d). Nevertheless, the seasonal and diurnal patterns in τ_{ice} remained robust against these uncertainty ranges, particularly during aphelion seasons when water-ice clouds were most abundant. Even during non-aphelion periods of elevated water-ice abundance, differences between morning and evening peaks in τ_{ice} and midday minima were often greater than mean nighttime uncertainties.

4.3 Spatial variability

Spatial maps of uncertainty-weighted mean τ_{ice} for 2-hour rolling-average periods during morning (centered at 07:00 LTST), midday (13:00 LTST), and late evening (22:00 LTST) are shown in Figure 7 for the three periods discussed previously. An animation showing these maps across all hours of the diurnal cycle is available online as Figure 8. During the daytime, development of water-ice clouds over volcanoes followed previously reported patterns (e.g., Atwood et al., 2022; Wolff et al., 2022), with formation beginning near midday and clouds growing in both spatial extent and optical depth throughout the afternoon. This pattern was evident not only during aphelion season but also during less dusty periods between regional dust storms, when τ_{ice} values often exceeded 0.7 in the vicinity of volcanoes.

Evening peaks in water-ice abundance showed considerable spatial variability, with τ_{ice} exceeding 0.7 across a range of longitudes and regions. The timing of this peak varied by region as well, with the Tharsis and volcano evening peaks observed closer to 18:00 LTST, while other regions (e.g. ~75°E longitude over Syrtis Major) included an evening peak in τ_{ice} closer to 22:00 LTST. This broad distribution of water-ice clouds in the evening was contrasted with the early morning hours between roughly 03:00 LTST and the morning peak around ~07:00 LTST—when the highest optical depths (exceeding 0.7) were concentrated over the Tharsis region, while other low-latitude clouds between roughly 30°E – 150°E longitude showed lower values around 0.4. During aphelion season, these early morning Tharsis ACB clouds extended from roughly 25°S to 45°N, indicating the substantial longitudinal enhancement of the morning ACB was largely due to clouds in the Tharsis region.

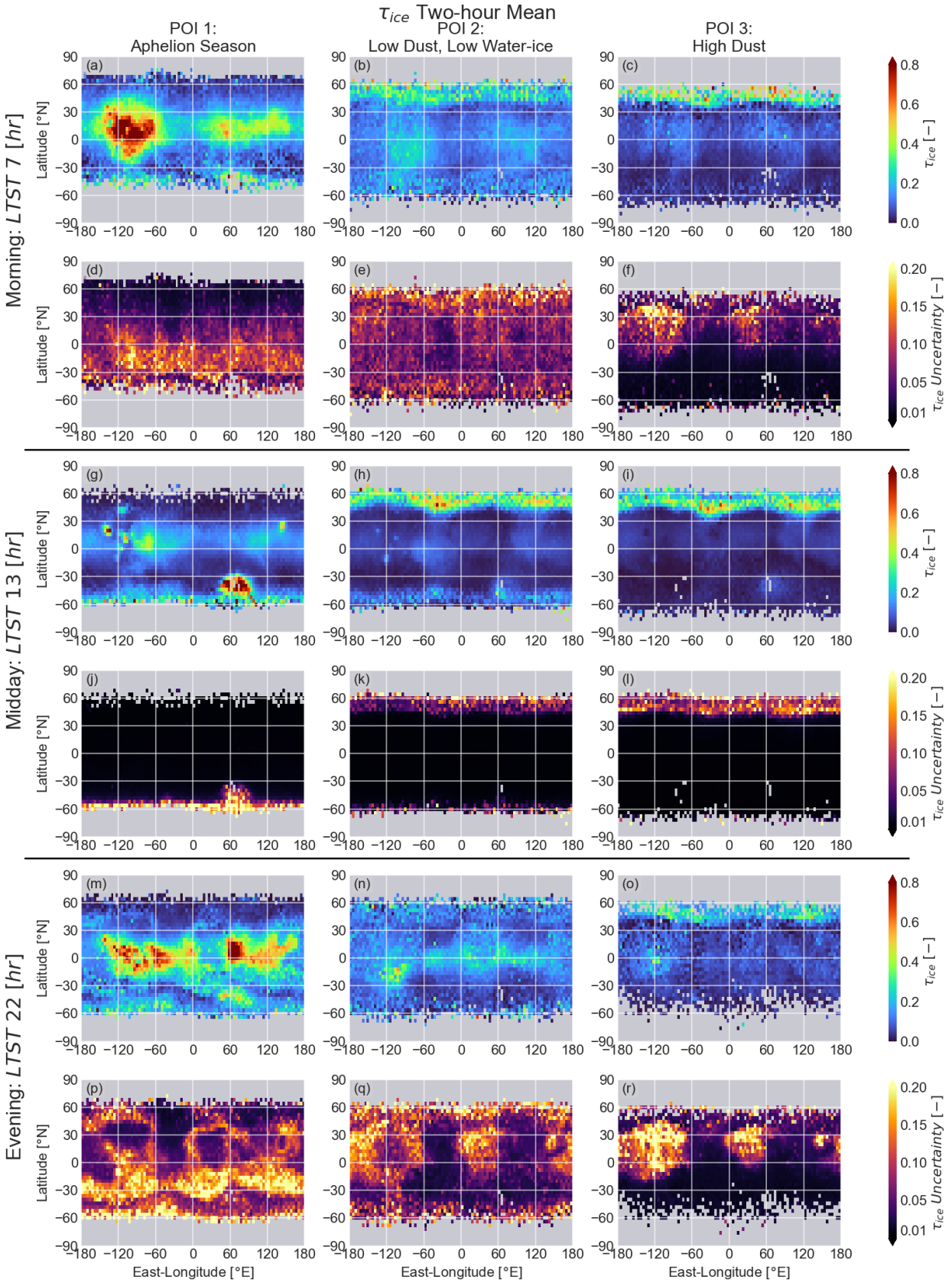
τ_{ice} Two-hour Mean
POI 1:
Aphelion Season
POI 2:
Low Dust, Low Water-ice
POI 3:
High Dust
Morning: LTST 7 [hr]
Midday: LTST 13 [hr]
Evening: LTST 22 [hr]
Latitude [°N]
East-Longitude [°E]
τ_{ice} [−]
τ_{ice} Uncertainty [−]
(a)
(b)
(c)
(d)
(e)
(f)
(g)
(h)
(i)
(j)
(k)
(l)
(m)
(n)
(o)
(p)
(q)
(r)

Figure 7 Spatial maps of 2-hr uncertainty-weighted mean EMIRS water-ice optical depth and mean uncertainty for the three periods of interest shown in Fig 3 and discussed in the text. Time periods shown here are for the morning peak in optical depth (diurnal maximum over Tharsis) at LTST=07:00 (top), midday diurnal minimum at LTST=13:00 (middle), and in the late evening at LTST=22:00 (bottom). Rolling 2-hr averages throughout the full diurnal cycle are shown as an animation in the online version in Fig 8.

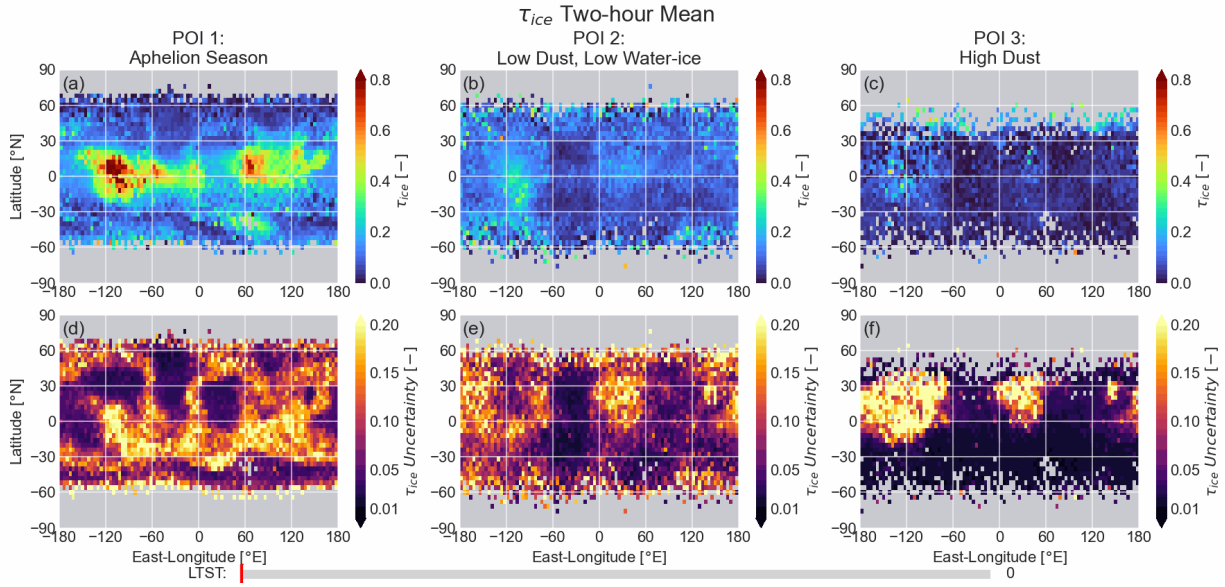

Figure 8 Spatial maps of 2-hr uncertainty-weighted mean EMIRS water-ice optical depth and mean uncertainty for the three periods of interest shown in Fig 3 and discussed in the text. Rolling 2-hr averages throughout the full diurnal cycle are shown as an animated version of Figure 7.

Mean uncertainties associated with nighttime retrievals revealed patterns related to surface thermophysical properties. As discussed in section 3.1, variable thermal inertia across different surface types lead to variability in τ_{ice} uncertainties at night. Higher uncertainties tended to occur in regions and at local times where decreased thermal contrast between the surface and atmosphere reduced sensitivity to water-ice spectral features.

4.4 Drivers of diurnal variability in τ_{ice}

Finally, the observed pattern of increased water ice abundance at night and peaks in τ_{ice} during morning and evening hours showed similarities to previous studies that have suggested such patterns may be due in part to thermal tide and topographic effects (e.g., Hinson & Wilson, 2004; Madeleine et al., 2012b; Kleinböhl et al., 2013; Wilson & Guzewich, 2014; Pottier et al., 2017; Szantai et al., 2021). Previous modeling work has indicated thermal tides as a likely driver of diurnal variability in water ice clouds, particularly through their influence on atmospheric temperatures that modulate conditions for cloud development. Modeling results from Hinson & Wilson (2004) found spatial patterns in τ_{ice} at 14:00 and 04:00 that were largely consistent with the EMIRS observations at these times, and attributed much of the differences in water-ice opacity between the two time periods to the effect of thermal tides. These studies have

highlighted feedback between radiatively active water-ice clouds, thermal tides, and topography as key potential drivers of diurnal variability in water-ice cloud abundance. While a detailed investigation of this relationship is beyond the scope of this work, we note that the spatial and temporal coverage in EMIRS results may allow for further investigation or validation of these feedbacks in models of the Martian atmosphere.

5 Comparison with other diurnal τ_{ice} observations

The Thermal InfraRed Sensor (TIRS) is a set of upward-looking radiometers onboard the Perseverance rover that measures downwelling thermal infrared radiation, enabling retrieval of aerosol optical depth at the low-latitude Jezero crater (18.4°N, 77.5°E) across the full diurnal cycle (Rodriguez-Manfredi et al., 2021; Smith et al., 2023). Recent analysis of nearly two Mars Years of TIRS observations (over a similar time period to the EMIRS dataset) has enabled separation of dust and water-ice contributions to total aerosol optical depth, and showed systematic variations in water-ice cloud abundance throughout day and night (Smith et al., 2025b). TIRS τ_{ice} retrievals demonstrated substantial consistency with the diurnal patterns observed by EMIRS over Syrtis Major near Perseverance (e.g, Figure 7 from Smith et al., 2025). During aphelion season, TIRS observed a strong evening peak in τ_{ice}, with values above 0.4 and often exceeding 0.5, and higher nighttime water-ice abundance compared to daytime values. Average EMIRS τ_{ice} in this region during aphelion season was in the range of 0.4 to 0.7 in the late evening between LTST 18 and 24. Substantial water-ice cloud formation was also observed during less dusty periods outside of aphelion season, with a pronounced morning peak that often occurred shortly after dawn and a separate late evening peak.

The Emirates eXploration Imager (EXI) onboard EMM provides complementary observations of water-ice clouds to EMIRS through UV and visible wavelength images of the Martian disk during daytime hours (Jones et al., 2021; Wolff et al., 2022). While EXI retrievals of τ_{ice} at 320 nm are not directly comparable in magnitude to EMIRS thermal infrared retrievals without consideration of additional water-ice particle properties such as effective radius, relative changes across spatial and temporal scales can be compared between instruments. EXI τ_{ice} retrievals also cannot distinguish between surface and atmospheric ice, and a surface ice mask was not applied to these results, leading to larger optical depths over the polar ice caps. Nevertheless, the two instruments showed general agreement in their observations of water-ice cloud variations across the diurnal cycle, particularly for the low- and mid-latitude clouds this analysis is focused on.

Figure 9 shows EMIRS and EXI τ_{ice} retrievals for five periods spanning different seasonal conditions during MY 36 and 37. During aphelion seasons, both instruments captured key features of the ACB, including the pronounced morning peak in cloud abundance and subsequent midday minimum. The latitudinal extension of early morning ACB clouds beyond typical daytime bounds was clearly evident in both datasets. Notably, during aphelion season both instruments showed the morning peak occurring shortly after sunrise, consistent with the ~75° solar incidence angle relationship discussed previously. During less dusty periods, similar patterns of diurnal cloud development were observed, though with reduced magnitude. The polar regions showed higher τ_{ice} in EXI observations compared to EMIRS—which may be partially attributed to surface ice effects or smaller particle sizes, though increased coverage further poleward in EXI results and lower thermal contrast and radiance in EMIRS observations over the poles may explain some of the discrepancies as well.

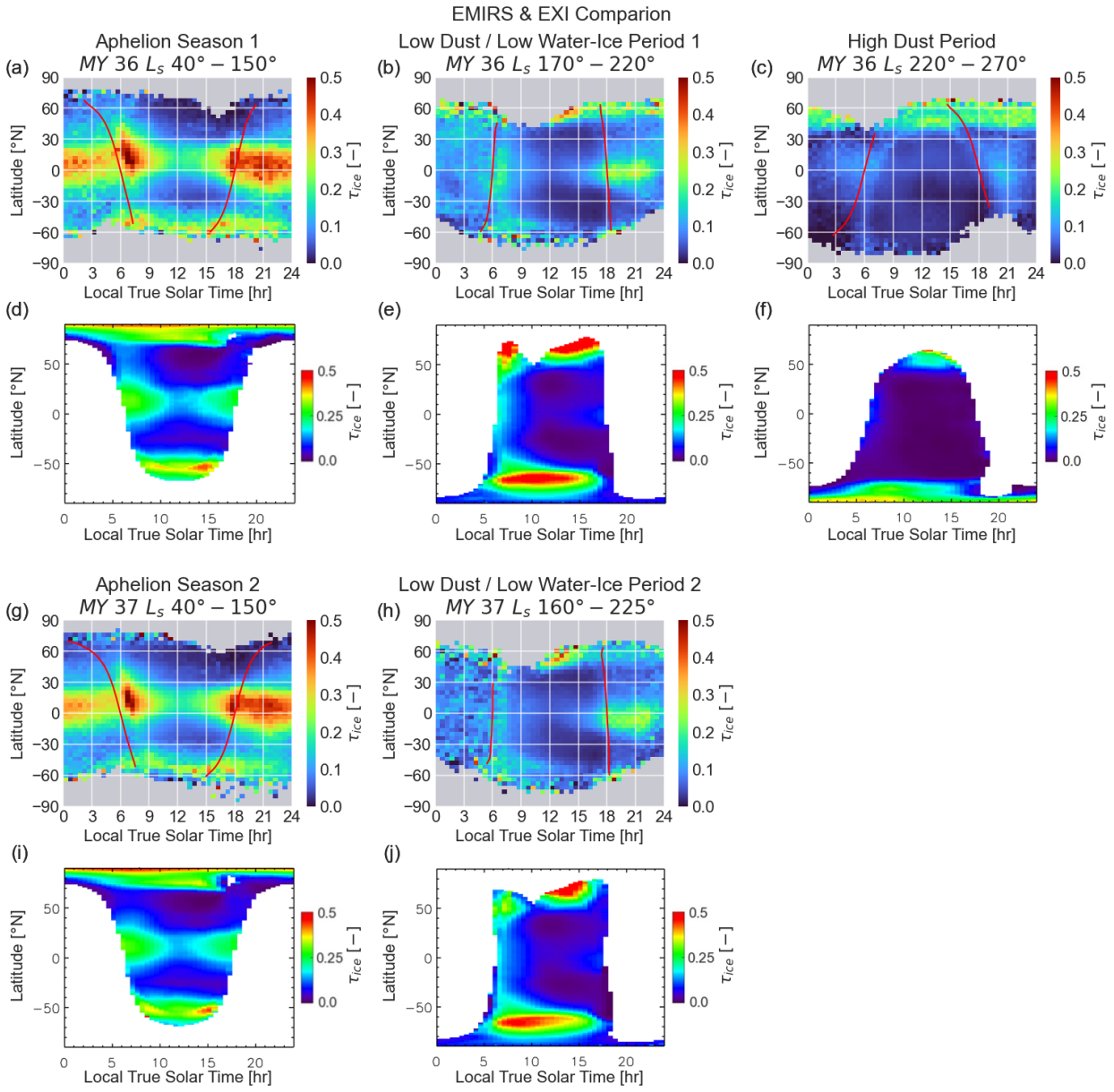

Figure 9 Zonal mean water-ice optical depth across the diurnal cycle for EMIRS (rows 1 and 3) and EXI (rows 2 and 4) retrievals across five periods of interest during MY 36 & 37. Red contour lines in EMIRS results show the 90° mean solar incidence angle (the day-night terminator). Note that EXI and EMIRS optical depths are referenced to different wavelengths and are not directly comparable in magnitude.

The consistency between EMIRS observations and both surface-based and orbital measurements provides additional validation of the diurnal behavior of water-ice clouds across different spatial scales and observational techniques. All three instruments captured the fundamental pattern of morning and evening peaks in cloud abundance separated by midday minima and higher nighttime τ_{ice} values, as well as persistent cloud activity during less dusty periods outside of aphelion. The timing of the morning peak shortly after dawn was particularly well-documented

across instruments, occurring near 75° solar incidence angle in EMIRS results, and occurring past sunrise in EXI and TIRS observations.

6 Conclusions

Understanding the full diurnal cycle of Mars' water ice clouds, particularly during nighttime hours when previous observations have been limited, is crucial for characterizing their role in the Martian climate system. This study presents the first detailed observations of the full diurnal cycle of water-ice clouds in the Martian atmosphere using thermal infrared spectra from EMIRS. The unique orbital configuration of EMM allowed for comprehensive observational coverage across all local times and nearly all latitudes and longitudes for nearly two Martian years. Updates to the retrieval algorithm, including improved treatment of surface thermophysical effects and inclusion of the 45-μm water ice band available in EMIRS observations, enabled retrieval of water ice optical depth throughout the full diurnal cycle. The result is a new τ_{ice} observational dataset with broad spatial and temporal coverage that includes nighttime hours.

Key findings of this study include:

- A persistent diurnal pattern in low- and mid-latitude clouds characterized by a midday minimum in τ_{ice}, with relative increases during both evening and early morning hours. The morning peak, which was often the highest optical depth in the diurnal cycle, consistently occurred shortly after dawn near a 75° solar incidence angle, across a range of latitudes and seasons.
- Across an aphelion season average, zonal mean τ_{ice} ranged from a maximum of ~0.5 in the morning to a minimum of ~0.15 near midday—consistent with previous TES midday observations around 14:00 LTST. Higher water-ice optical depths were observed at night compared to midday throughout much of the year, with particularly pronounced differences during aphelion season when ACB clouds were often more than twice their midday minimum values.
- Substantial spatial variability was observed in nighttime cloud patterns, with evening clouds at low- and mid-latitudes distributed across more longitudinal regions, while the most abundant early morning clouds tended to occur over the Tharsis region. The ACB reached considerably wider latitudinal extents in the early morning hours, particularly over Tharsis where clouds extended from roughly 25°S to 45°N—well beyond typical midday bounds.
- Detection of considerable water ice cloud abundance outside of aphelion season during less dusty periods between regional dust storms—particularly at night and during morning and evening peaks. Mean τ_{ice} values of ~0.2 were commonly observed during these periods, revealing cloud activity that was often not apparent in previous datasets limited to near-midday observations.

Comparisons with TIRS and EXI observations showed good agreement in the diurnal patterns of cloud development, providing similar observations of key features including the post-dawn morning peak in cloud abundance. The observed diurnal patterns also showed notable similarities to those expected from the influence of atmospheric thermal tides on cloud formation conditions, though detailed investigation of this relationship requires further study. The comprehensive diurnal coverage presented here offers new constraints on water-ice cloud

abundance for atmospheric models and an improved understanding of the role of water-ice clouds in the Martian climate system. Future work will focus on detailed investigation of the drivers of cloud development, including how thermal tides and topography modulate cloud formation and create feedbacks with atmospheric temperatures, and the implications for atmospheric transport and the global water cycle.

Acknowledgments

The material is based upon work supported by NASA under award number 80GSFC24M0006. We would also like to acknowledge and thank the reviewers for their helpful suggestions regarding descriptions of EMIRS uncertainties and classification of the periods of interest.

Open Research

Data from the Emirates Mars Mission and EMIRS are freely and publicly available on the EMM Science Data Center (SDC, http://sdc.emiratesmarsmission.ae). Relevant results from this work, including retrieval output and uncertainty weighted mean values for water-ice optical depths, have been saved as NetCDF4 files and archived on Mendeley Data (Atwood, 2025).

References

Almatroushi, H., AlMazmi, H., AlMheiri, N., AlShamsi, M., AlTunaiji, E., Badri, K., et al. (2021). Emirates Mars Mission Characterization of Mars Atmosphere Dynamics and Processes. *Space Science Reviews*, *217*(8), 89. https://doi.org/10.1007/s11214-021-00851-6

Amiri, H. E. S., Brain, D., Sharaf, O., Withnell, P., McGrath, M., Alloghani, M., et al. (2022). The Emirates Mars Mission. *Space Science Reviews*, *218*(1), 4. https://doi.org/10.1007/s11214-021-00868-x

Atwood, S. A. (2025). EMIRS water-ice cloud optical depth retrievals across the full diurnal cycle at Mars (Version 1) [Data set]. Mendeley Data. https://doi.org/10.17632/yhk4tzbcd5.1

Atwood, S. A., Smith, M. D., Badri, K., Edwards, C. S., Christensen, P. R., Wolff, M. J., et al. (2022). Diurnal Variability in EMIRS Daytime Observations of Water Ice Clouds During Mars Aphelion-Season. *Geophysical Research Letters*, *49*(15), e2022GL099654. https://doi.org/10.1029/2022GL099654

Atwood, S. A., Smith, M. D., Wolff, M. J., Badri, K., Edwards, C. S., Christensen, P. R., et al. (2024). Spatial and temporal variability of martian water-ice cloud effective radius in EMIRS thermal infrared observations. *Icarus*, *418*, 116148. https://doi.org/10.1016/j.icarus.2024.116148

Bandfield, J. L. (2002). Global mineral distributions on Mars. *Journal of Geophysical Research: Planets*, *107*(E6), 9-1-9–20. https://doi.org/10.1029/2001JE001510

Bandfield, J. L. (2009). Effects of surface roughness and graybody emissivity on martian thermal infrared spectra. *Icarus*, *202*(2), 414–428. https://doi.org/10.1016/j.icarus.2009.03.031

Bandfield, J. L., & Edwards, C. S. (2008). Derivation of martian surface slope characteristics from directional thermal infrared radiometry. *Icarus*, *193*(1), 139–157. https://doi.org/10.1016/j.icarus.2007.08.028

Barnes, J. R., Haberle, R. M., Wilson, R. J., Lewis, S. R., Murphy, J. R., & Read, P. L. (2017). The Global Circulation. In *The Atmosphere and Climate of Mars*. Cambridge University Press.

Benson, J. L., Bonev, B. P., James, P. B., Shan, K. J., Cantor, B. A., & Caplinger, M. A. (2003). The seasonal behavior of water ice clouds in the Tharsis and Valles Marineris regions of Mars: Mars Orbiter Camera Observations. *Icarus*, *165*(1), 34–52. https://doi.org/10.1016/S0019-1035(03)00175-1

Clancy, R. T., Montmessin, F., Benson, J. L., Daerden, F., Colaprete, A., & Wolff, M. J. (2017). Mars Clouds. In *The Atmosphere and Climate of Mars*. Cambridge University Press.

Conrath, B. J., Pearl, J. C., Smith, M. D., Maguire, W. C., Christensen, P. R., Dason, S., & Kaelberer, M. S. (2000). Mars Global Surveyor Thermal Emission Spectrometer (TES) observations: Atmospheric temperatures during aerobraking and science phasing. *Journal of Geophysical Research: Planets*, *105*(E4), 9509–9519. https://doi.org/10.1029/1999JE001095

Curran, R. J., Conrath, B. J., Hanel, R. A., Kunde, V. G., & Pearl, J. C. (1973). Mars: Mariner 9 Spectroscopic Evidence for H2O Ice Clouds. *Science*, *182*(4110), 381–383. https://doi.org/10.1126/science.182.4110.381

Edwards, C. S., Christensen, P. R., Mehall, G. L., Anwar, S., Tunaiji, E. A., Badri, K., et al. (2021). The Emirates Mars Mission (EMM) Emirates Mars InfraRed Spectrometer (EMIRS) Instrument. *Space Science Reviews*, *217*(7), 77. https://doi.org/10.1007/s11214-021-00848-1

French, R. G., Gierasch, P. J., Popp, B. D., & Yerdon, R. J. (1981). Global patterns in cloud forms on Mars. *Icarus*, *45*(2), 468–493. https://doi.org/10.1016/0019-1035(81)90047-6

Giuranna, M., Wolkenberg, P., Grassi, D., Aronica, A., Aoki, S., Scaccabarozzi, D., et al. (2021). The current weather and climate of Mars: 12 years of atmospheric monitoring by the Planetary Fourier Spectrometer on Mars Express. *Icarus*, *353*, 113406. https://doi.org/10.1016/j.icarus.2019.113406

Hayes, C. W., Kloos, J. L., Innanen, A. C., Campbell, C. L., Sapers, H. M., & Moores, J. E. (2024). Five Mars Years of Cloud Observations at Gale Crater: Opacities, Variability, and Ice Crystal Habits. *The Planetary Science Journal*, *5*(2), 51. https://doi.org/10.3847/PSJ/ad2202

Hinson, D. P., & Wilson, R. J. (2004). Temperature inversions, thermal tides, and water ice clouds in the Martian tropics. *Journal of Geophysical Research: Planets*, *109*(E1). https://doi.org/10.1029/2003JE002129

Jakosky, B. M., Mellon, M. T., Kieffer, H. H., Christensen, P. R., Varnes, E. S., & Lee, S. W. (2000). The thermal inertia of Mars from the Mars Global Surveyor Thermal Emission Spectrometer. *Journal of Geophysical Research: Planets*, *105*(E4), 9643–9652. https://doi.org/10.1029/1999JE001088

Jones, A. R., Wolff, M., Alshamsi, M., Osterloo, M., Bay, P., Brennan, N., et al. (2021). The Emirates Exploration Imager (EXI) Instrument on the Emirates Mars Mission (EMM) Hope Mission. *Space Science Reviews*, *217*(8), 81. https://doi.org/10.1007/s11214-021-00852-5

Kahn, R. (1984). The spatial and seasonal distribution of Martian clouds and some meteorological implications. *Journal of Geophysical Research: Space Physics*, *89*(A8), 6671–6688. https://doi.org/10.1029/JA089iA08p06671

Kleinböhl, A., John Wilson, R., Kass, D., Schofield, J. T., & McCleese, D. J. (2013). The semidiurnal tide in the middle atmosphere of Mars. *Geophysical Research Letters*, *40*(10), 1952–1959. https://doi.org/10.1002/grl.50497

Kloos, J. L., Moores, J. E., Whiteway, J. A., & Aggarwal, M. (2018). Interannual and Diurnal Variability in Water Ice Clouds Observed from MSL Over Two Martian Years. *Journal of Geophysical Research: Planets*, *123*(1), 233–245. https://doi.org/10.1002/2017JE005314

Määttänen, A., & Montmessin, F. (2021). Clouds in the Martian Atmosphere. In *Oxford Research Encyclopedia of Planetary Science*. https://doi.org/10.1093/acrefore/9780190647926.013.114

Madeleine, J.-B., Forget, F., Spiga, A., Wolff, M. J., Montmessin, F., Vincendon, M., et al. (2012a). Aphelion water-ice cloud mapping and property retrieval using the OMEGA imaging spectrometer onboard Mars Express. *Journal of Geophysical Research: Planets*, *117*(E11). https://doi.org/10.1029/2011JE003940

Madeleine, J.-B., Forget, F., Millour, E., Navarro, T., & Spiga, A. (2012b). The influence of radiatively active water ice clouds on the Martian climate. *Geophysical Research Letters*, *39*(23). https://doi.org/10.1029/2012GL053564

Michaels, T. I., Colaprete, A., & Rafkin, S. C. R. (2006). Significant vertical water transport by mountain-induced circulations on Mars. *Geophysical Research Letters*, *33*(16). https://doi.org/10.1029/2006GL026562

Montmessin, F., Smith, M. D., Langevin, Y., Mellon, M. T., & Fedorova, A. (2017). The Water Cycle. In *The Atmosphere and Climate of Mars*. Cambridge University Press.

Navarro, T., Madeleine, J.-B., Forget, F., Spiga, A., Millour, E., Montmessin, F., & Määttänen, A. (2014). Global climate modeling of the Martian water cycle with improved microphysics and radiatively active water ice clouds. *Journal of Geophysical Research: Planets*, *119*(7), 1479–1495. https://doi.org/10.1002/2013JE004550

Nowicki, S. A., & Christensen, P. R. (2007). Rock abundance on Mars from the Thermal Emission Spectrometer. *Journal of Geophysical Research: Planets*, *112*(E5). https://doi.org/10.1029/2006JE002798

Olsen, K. S., Forget, F., Madeleine, J.-B., Szantai, A., Audouard, J., Geminale, A., et al. (2021). Retrieval of the water ice column and physical properties of water-ice clouds in the martian atmosphere using the OMEGA imaging spectrometer. *Icarus*, *353*, 113229. https://doi.org/10.1016/j.icarus.2019.03.006

Pankine, A. A., Tamppari, L. K., Bandfield, J. L., McConnochie, T. H., & Smith, M. D. (2013). Retrievals of martian atmospheric opacities from MGS TES nighttime data. *Icarus*, *226*(1), 708–722. https://doi.org/10.1016/j.icarus.2013.06.024

Patel, P., Tamppari, L., Juárez, M. de la T., Lemmon, M., Coates, A., Wolff, M., et al. (2023). Geometric Properties of Water-ice Clouds as Observed from Jezero Crater in the First 600 sols with the NavCam Instrument On Board the Mars2020 Rover, Perseverance. *The Planetary Science Journal*, *4*(12), 226. https://doi.org/10.3847/PSJ/acfc35

Pearl, J. C., Smith, M. D., Conrath, B. J., Bandfield, J. L., & Christensen, P. R. (2001). Observations of Martian ice clouds by the Mars Global Surveyor Thermal Emission Spectrometer: The first Martian year. *Journal of Geophysical Research: Planets*, *106*(E6), 12325–12338. https://doi.org/10.1029/1999JE001233

Pottier, A., Forget, F., Montmessin, F., Navarro, T., Spiga, A., Millour, E., et al. (2017). Unraveling the martian water cycle with high-resolution global climate simulations. *Icarus*, *291*, 82–106. https://doi.org/10.1016/j.icarus.2017.02.016

Putzig, N. E., & Mellon, M. T. (2007). Apparent thermal inertia and the surface heterogeneity of Mars. *Icarus*, *191*(1), 68–94. https://doi.org/10.1016/j.icarus.2007.05.013

Rodriguez-Manfredi, J. A., de la Torre Juárez, M., Alonso, A., Apéstigue, V., Arruego, I., Atienza, T., et al. (2021). The Mars Environmental Dynamics Analyzer, MEDA. A Suite of Environmental Sensors for the Mars 2020 Mission. *Space Science Reviews*, *217*(3), 48. https://doi.org/10.1007/s11214-021-00816-9

Smith, M. D. (2004). Interannual variability in TES atmospheric observations of Mars during 1999–2003. *Icarus*, *167*(1), 148–165. https://doi.org/10.1016/j.icarus.2003.09.010

Smith, M. D. (2009). THEMIS observations of Mars aerosol optical depth from 2002–2008. *Icarus*, *202*(2), 444–452. https://doi.org/10.1016/j.icarus.2009.03.027

Smith, M. D. (2019). Local time variation of water ice clouds on Mars as observed by THEMIS. *Icarus*, *333*, 273–282. https://doi.org/10.1016/j.icarus.2019.06.009

Smith, M. D., Wolff, M. J., Spanovich, N., Ghosh, A., Banfield, D., Christensen, P. R., et al. (2006). One Martian year of atmospheric observations using MER Mini-TES. *Journal of Geophysical Research: Planets*, *111*(E12). https://doi.org/10.1029/2006JE002770

Smith, M. D., Badri, K., Atwood, S. A., Edwards, C. S., Christensen, P. R., Wolff, M. J., et al. (2022). EMIRS Observations of the Aphelion-Season Mars Atmosphere. *Geophysical Research Letters*, *49*(15), e2022GL099636. https://doi.org/10.1029/2022GL099636

Smith, M. D., Martínez, G. M., Sebastián, E., Lemmon, M. T., Wolff, M. J., Apéstigue, V., et al. (2023). Diurnal and Seasonal Variations of Aerosol Optical Depth Observed by MEDA/TIRS at Jezero Crater, Mars. *Journal of Geophysical Research: Planets*, *128*(1), e2022JE007560. https://doi.org/10.1029/2022JE007560

Smith, M. D., Atwood, S. A., Badri, K., & Edwards, C. S. (2025a). The Diurnal cycles of dust and water vapor as observed by EMIRS. *Journal of Geophysical Research: Planets*. https://doi.org/10.1029/2025JE008972

Smith, M. D., Martínez, G. M., Sebastián, E., Lemmon, M. T., Atwood, S. A., Toledo, D., et al. (2025b). The diurnal variation of dust and water ice aerosol optical depth at Jezero crater observed by MEDA/TIRS over a full Martian year. *Icarus*, *425*, 116313. https://doi.org/10.1016/j.icarus.2024.116313

Szantai, A., Audouard, J., Forget, F., Olsen, K. S., Gondet, B., Millour, E., et al. (2021). Martian cloud climatology and life cycle extracted from Mars Express OMEGA spectral images. *Icarus*, *353*, 114101. https://doi.org/10.1016/j.icarus.2020.114101

Tamppari, L. K., Zurek, R. W., & Paige, D. A. (2003). Viking-era diurnal water-ice clouds. *Journal of Geophysical Research: Planets*, *108*(E7). https://doi.org/10.1029/2002JE001911

Wilson, R. J., & Guzewich, S. D. (2014). Influence of water ice clouds on nighttime tropical temperature structure as seen by the Mars Climate Sounder. *Geophysical Research Letters*, *41*(10), 3375–3381. https://doi.org/10.1002/2014GL060086

Wilson, R. J., Neumann, G. A., & Smith, M. D. (2007). Diurnal variation and radiative influence of Martian water ice clouds. *Geophysical Research Letters*, *34*(2). https://doi.org/10.1029/2006GL027976

Wolff, M. J., Clancy, R. T., Kahre, M. A., Haberle, R. M., Forget, F., Cantor, B. A., & Malin, M. C. (2019). Mapping water ice clouds on Mars with MRO/MARCI. *Icarus*, *332*, 24–49. https://doi.org/10.1016/j.icarus.2019.05.041

Wolff, M. J., Fernando, A., Smith, M. D., Forget, F., Millour, E., Atwood, S. A., et al. (2022). Diurnal Variations in the Aphelion Cloud Belt as Observed by the Emirates Exploration Imager (EXI). *Geophysical Research Letters*, *49*(18), e2022GL100477. https://doi.org/10.1029/2022GL100477

Zurek, R. W. (1976). Diurnal tide in the Martian atmosphere. *Journal of the Atmospheric Sciences*, *33*(2), 321–337.